Highlights

Dipole- and vortex sheet-based models of fish swimming

Peng Zhang,Sean D. Peterson,Maurizio Porfiri

- Potential flow offers a viable framework for modeling fish swimming
- Experimental data are used to create a model of zebrafish body undulations
- Computational fluid dynamics is employed to validate dipole-based swimming models
- Dipole-based models capture the main flow features at a limited computational cost
- Further improvement is obtained through the use of vortex sheets

Dipole- and vortex sheet-based models of fish swimming

Peng Zhang[a,b], Sean D. Peterson[c] and Maurizio Porfiri[d,*]

[a]Department of Mechanical and Aerospace Engineering and Center for Urban Science and Progress, New York University Tandon School of Engineering, 370 Jay Street, Brooklyn, 11201, NY, USA

[b]Department of Mechanical Engineering, Tennessee Tech University, 115 W. 10th Street, Cookeville, 38505, TN, USA

[c]Mechanical and Mechatronics Engineering Department, University of Waterloo, 200 University Avenue West, Waterloo, N2L 3G1, ON, Canada

[d]Department of Mechanical and Aerospace Engineering, Department of Biomedical Engineering, and Center for Urban Science and Progress, New York University Tandon School of Engineering, 370 Jay Street, Brooklyn, 11201, NY, USA

ARTICLE INFO

Keywords:
CFD
dipole
hydrodynamics
locomotion
potential flow

ABSTRACT

Elucidating the hydrodynamics of fish swimming is critical to identifying the processes underlying fish orientation and schooling. Due to their mathematical tractability, models based on potential flow are preferred in the study of bidirectional interactions of fish with their surroundings. Dipole-based models that assimilate fish to pairs of vortices are particularly enticing, but yet to be thoroughly validated. Here, we embark on a computational fluid dynamics (CFD) campaign informed by experimental data to validate the accuracy of dipole-based models. The locomotory patterns of a fish undergoing carangiform swimming are reconstructed from existing experimental data, which are used as inputs to CFD simulations of a fish swimming in a channel flow. We demonstrate that dipole-based models are accurate in capturing key features of the fluid flow, but cannot predict the elongated flow streamlines around the fish that are evident in CFD. To address this issue, we propose an alternative model that replaces each vortex in the pair with a sheet along the fish length. Using a pair of vortex sheets that span approximately 80% of the fish body length with a separation distance of approximately 50% of the body width, the model is successful in predicting the fluid flow around the swimming fish for a range of background flow speeds and channel widths. The proposed model shows improved accuracy at the cost of a mildly increased computational effort, thereby constituting an ideal basis for research on fish hydrodynamics.

1. Introduction

Hydrodynamics plays an essential role in fish behavior (Liao, 2007). From the orientation against incoming currents (Coombs, Bak-Coleman and Montgomery, 2020) to coordinated swimming in schools (Pitcher, 1998; Pavlov and Kasumyan, 2000), hydrodynamic cues are critical for fish to interact with their surroundings. To date, several efforts have been devoted to the development of hydrodynamic models of swimming fish (Triantafyllou, Triantafyllou and Yue, 2000; Wu, 2011), spanning computational fluid dynamics (CFD) (Adkins and Yan, 2006; Takagi, Tamura and Weihs, 2013; Hemelrijk, Reid, Hildenbrandt and Padding, 2015; Doi, Takagi, Mitsunaga and Torisawa, 2021) and simplified mathematical models (Lighthill, 1970, 1971; Wu, 1971; Katz and Weihs, 1978; Hassan, 1985; Ysasi, Kanso and Newton, 2011; Tchieu, Kanso and Newton, 2012; Iosilevskii, 2016).

CFD offers a vantage point to detail the flow physics in the vicinity of a swimming animal and in the far-field (Adkins and Yan, 2006; Takagi et al., 2013; Hemelrijk et al., 2015; Doi et al., 2021). For example, Adkins and Yan (2006) performed a three-dimensional CFD study of a fish-like swimmer in a viscous flow; Takagi et al. (2013) conducted an equivalent analysis to quantify energetic costs of different swimming patterns; and Hemelrijk et al. (2015) and Doi et al. (2021) studied energy savings in swimming schools through two-dimensional and three-dimensional simulations, respectively.

Despite the high degree of resolution that can be achieved through CFD simulations, computational costs challenge their systematic use for the study of large fish schools, which become computationally intractable. While two-dimensional CFD simulations of a single fish swimming for a few tail beating cycles could require a total CPU time on the order of tens of hours using modern computers, more complex simulations involving multiple individuals, three-dimensional phenomena, and extended observation windows would strain typical computational resources and call for state-of-the art solutions in scientific computing (Khan, Ruiz Hussmann, Powalla, Hoerner, Kruusmaa and Tuhtan,

mporfiri@nyu.edu (M. Porfiri)
ORCID(s): 0000-0001-8237-1259 (P. Zhang); 0000-0001-8746-2491 (S.D. Peterson); 0000-0002-1480-3539 (M. Porfiri)

2022). Likewise, CFD simulations are difficult to adapt to study bidirectional interactions between the swimming animal and the surrounding fluid flow; in these instances, the motion of the fish cannot be *a priori* imposed as routinely posited within existing CFD studies. Instead, models that incorporate bidirectional fish-fluid interactions should consider the influence of the flow environment on the activation of the muscles in the fish body, which could contain intrinsic nonlinearities that challenge the accurate identification of the muscle forces (Tytell, Hsu, Williams, Cohen and Fauci, 2010; Hamlet, Fauci and Tytell, 2015).

Simplified mathematical models based on potential flow theory constitute a viable approach to analytically study fish hydrodynamics and overcome some of the current limitations of CFD technology. The most celebrated mathematical model of fish swimming dates back to the seminal work of Lighthill on the elongated-body theory, which helped illuminate the principles of fish propulsion for small (Lighthill, 1970) and large body undulations (Lighthill, 1971). Since the work of Lighthill, several authors have developed simplified models of swimming (Wu, 1971; Katz and Weihs, 1978; Hassan, 1985; Ysasi et al., 2011).

A particularly elegant and promising class of idealized model is the "finite-dipole" paradigm, proposed by Tchieu et al. for the study of two-dimensional swimming (Tchieu et al., 2012). Within the finite-dipole paradigm, the flow field around a fish is modeled by a pair of point vortices with equal and opposite circulations, separated by a finite distance. The model predicts a flow pattern from one side of the dipole to the other end, which is reminiscent of experimental visualization of the flow around a fish swimming in a channel (Windsor, Norris, Cameron, Mallinson and Montgomery, 2010a,b).

The simple mathematical form of the finite-dipole model makes it possible to derive an analytical expression of the fluid flow, upon which multiple authors have provided insight into important aspects of fish swimming. For example, Gazzola, Tchieu, Alexeev, de Brauer and Koumoutsakos (2016) studied interactions among multiple fish, leading to the discovery of optimal fish school patterns. Burbano-L. and Porfiri (2021) formulated a model of fish orientation that helped clarify the role of hydrodynamic cues against visual stimuli. Interestingly, the finite-dipole model can be further simplified into a point-dipole representation when focusing on the far-field flow. Such a point-dipole representation was recently employed to study the role of the channel walls on fish orientation (Porfiri, Zhang and Peterson, 2022), analyze the stability of tandem swimming in fish pairs (Porfiri, Karakaya, Sattanapalle and Peterson, 2021), and predict schooling patterns of large groups (Filella, Nadal, Sire, Kanso and Eloy, 2018).

Despite the promise of dipole-based models, limited efforts have been devoted to the validation of the accuracy of such a modeling framework; to the best of our knowledge, the only, partial, preliminary validation of a dipole-based model has been recently attempted by Porfiri et al. (2022). In this vein, the implications of some of the key approximations of the paradigm remain understudied. For example, the model ignores the inertia of the fish, such that fish respond to the flow instantaneously, which is in contrast with intuition and experimental observations (Hunter, 1969; Pitcher, Partridge and Wardle, 1976). In addition, the model ignores the body shape and size of the animal, so that it should be strictly valid away from the animal, deep into the far-field (Tchieu et al., 2012). Unlike the elongated-body theory of Lighthill (1970, 1971), the model does not account for the role of the viscous boundary layer, which would support flow separation and vortex shedding in the wake – both absent in dipole-based models. These limitations could hinder a faithful representation of flow field and fish behavior, warranting further investigations about the accuracy of dipole-based models.

Our effort has a twofold objective. The first objective of the current study is to validate the accuracy of dipole-based models in predicting the hydrodynamics of fish swimming. To this end, we pursue a numerical framework based on CFD informed by experimental data. Specifically, the locomotory patterns of a model fish species, zebrafish, is extracted from previous experimental recordings (Mwaffo, Zhang, Cruz and Porfiri, 2017). The experimental data are used to construct a locomotory model of a fish in a channel flow, which is incorporated into a laminar flow-based CFD solver to study the time-resolved flow field around the fish. Grounded in these numerical results, we evaluate the accuracy of the predicted velocity field by dipole-based models. The comparison is carried out with respect to the mean flow predicted by CFD simulations, consistent with the steady-state representation of simplified mathematical models that offer a leading order approximation of the flow in the far field. CFD simulations provide important insight into the error associated with such a representation, including the absence of a wake structure in dipole-based models.

By acknowledging discrepancies between numerical and analytical results, the second objective of this manuscript is to propose an improved version of the finite-dipole paradigm to better capture flow patterns in the near-field. Such flow patterns entail the streamlines around the fish body that should be axially elongated (Windsor et al., 2010a,b). To encapsulate the geometry of the fish body, we propose the use of vortex sheets. Assimilating the fish body to a vortex sheet has been attempted by Wu (1971) in a classical study on the undulations of a thin ribbon plate, continuously

Table 1
Mean values of the fitting parameters in Eq. (1) determined based on the locomotory patterns of five fish.

Parameters	c_0	c_1	c_2	c_3	k_L	$2\pi f$
Fitted values	3.00×10^{-3}	2.06×10^{-2}	-4.05×10^{-2}	9.76×10^{-2}	7.00	54.32 Hz

generating vorticity on its surface. Similar to the validation of dipole-based models, we focus on the mean flow, rather than the unsteady wake structure as considered by the model by Wu (1971). Hence, we do not consider vorticity shedding in the wake and hypothesize the existence of two vortex sheets of equal and opposite strengths separated by a finite distance of the order of the fish width. The accuracy of the model is assessed by comparing the predicted velocity field with CFD results.

The rest of the paper is organized as follows. In Sec. 2, we describe the proposed numerical framework, with details on the implementation of the fish swimming and CFD simulations. In Sec. 3, we present the analytical expressions of the velocity field associated with the finite-dipole, the point-dipole, and the vortex sheet-based model. Major findings are presented in Sec. 4. Discussions and suggestions for future work are summarized in Sec. 5.

2. Numerical simulations

2.1. Locomotory patterns of swimming fish

Locomotory patterns of zebrafish are available from our previous work (Mwaffo et al., 2017). Therein, high speed videos of zebrafish swimming in a water channel of diameter $W = 4.57$ cm and length $L_t = 15.0$ cm were recorded at 160 frames per second. Among them, we identified episodes of steady swimming of five individual fish in a background flow at a speed of 2.6 cm/s. The body shape of the fish was extracted from each frame of the video through tracking the centerline of the fish body using a custom-built image analysis program in the commercial software MATLAB.

As illustrated in Fig. 1, zebrafish undulate their body during steady swimming: their head undergoes minimal movement and the oscillation amplitude increases along the body, peaking near the caudal fin. This locomotory pattern is similar to the one observed in mullet, typically classified as "carangiform" (Sfakiotakis, Lane and Davies, 1999; Hemelrijk et al., 2015). A simplified, mathematical representation of carangiform swimming consists of a traveling wave along the body with increasing oscillation amplitude from the head to the tail (Cheng and Blickhan, 1994; Liu and Hu, 2010; Reid, Hildenbrandt, Padding and Hemelrijk, 2012; Hemelrijk et al., 2015; Curatolo and Teresi, 2016). Specifically, we express the body shape of zebrafish as

$$\Delta y(x,t) = \left(c_0 + c_1\left(\frac{x}{L}\right) + c_2\left(\frac{x}{L}\right)^2 + c_3\left(\frac{x}{L}\right)^3\right)\sin\left(k_L\frac{x}{L} - \omega\frac{t}{T}\right). \tag{1}$$

Here, x is the coordinate along the axial direction, as shown in Fig. 1(a); $\Delta y(x,t)$ is the lateral displacement of the centerline of the fish body at x and time t; $L = 3.55$ cm is the mean body length of the five fish included in our analysis; c_i $(i = 0, 1, \cdots, 3)$ are coefficients of the polynomials that defines the envelope of the undulation profiles; $k_L = 2\pi L/\lambda$ is the non-dimensional wavenumber representing the number of complete sinusoidal waves along the body, where λ is the wavelength; and $\omega = 2\pi fT$ is the non-dimensional angular oscillation frequency, where f is the fish tail beating frequency, $T = L/U$ is the characteristic convective time, and U is the speed of the fish.

Compared with the locomotory pattern adopted in previous studies (Liu and Hu, 2010; Reid et al., 2012; Hemelrijk et al., 2015), in Eq. (1), we included an additional cubic term in the polynomial in x to account for the large stroke observed near the caudal fin of zebrafish (see Fig. 1(a)). Equation (1) is fitted to the experimental data by treating $\Delta y(x,t)$ as a dependent variable, x and t as independent variables, and c_i $(i = 0, 1, \cdots, 3)$, k_L, and $(2\pi f)$ as fitting parameters. Least square fitting of Eq. (1) to experimental data was achieved through the built-in MATLAB function "fit". Mean values of the fitting parameters determined based on the locomotory patterns of five fish are presented in Table 1. An exemplary series of fitted centerline profiles are displayed in Fig. 1(a).

The outline of the undeformed fish body was approximated by a NACA0011 airfoil. A NACA0011 airfoil has a maximum thickness-to-chord ratio of 11%, which is chosen based on the body width-to-length ratio, b/L, of the zebrafish considered in our analysis, where $b = 3.79$ mm is the maximum body width. A locomotory model for zebrafish can be constructed by combining the outline of the fish body with the centerline undulation described in Eq. (1), where the fitting parameters are averaged over the five fish considered in our analysis. Snapshots of the fish body shape during an oscillation period are exhibited in Fig. 1(b).

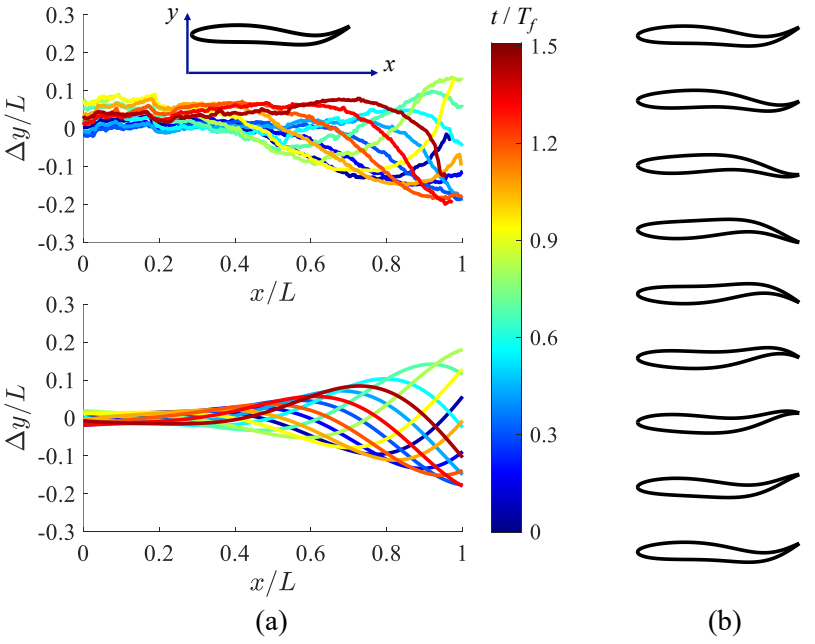

Figure 1: (a) Example of fish centerline profiles extracted from experimental recordings (top) and their fitted shapes through Eq. (1) (bottom). Colorbar represents time scaled by the tail beating period, $T_f = 1/f$. (b) Snapshots of the modeled fish body shapes at nine successive instances during an oscillation period.

2.2. Computational framework

A two-dimensional CFD framework was created to simulate the flow physics around a fish swimming in a channel flow. The premise of a CFD-based approach for the validation of hydrodynamic models of fish swimming has been explored in Porfiri et al. (2022), which demonstrated qualitative agreement between the mean flow created by a dipole and the one associated with a swimming giant danio. The computational effort in this manuscript expands on this preliminary finding and provides an in-depth, quantitative comparison between dipole- and vortex sheet-based hydrodynamic models of fish swimming.

A computational domain was created around the geometric model of swimming zebrafish constructed in Sec. 2.1. The dimensions of the computational domain were selected based on the size of the experimental test section in Mwaffo et al. (2017). The width of the computational domain was the same as the diameter of the water channel, W, while its length was twice the length of the channel, $2L_t$. The computational domain was intentionally enlarged along the axial direction to fully capture the flow structures generated in the wake of the fish (see Fig. 2(a)).

At the inlet of the domain, we imposed a uniform velocity U. We applied a slip-wall boundary condition on the side walls of the domain, where the normal velocity is prescribed to be zero to satisfy the non-penetration condition, while the viscous boundary layers are neglected. This assumption is expected to be valid at the flow conditions considered in our study, where the Reynolds number for the channel flow, $\mathrm{Re} = WU/\nu$, is of the order of 10^4. A zero-pressure condition was set at the outlet of the domain. The locomotory model of fish shown in Fig. 1(b) was imported into the computational domain. The axial movement of the fish body along the channel was set to zero and the lateral movement about the center of the channel was prescribed by Eq. (1), with fitting parameters identified from experimental data. The time-varying shape of the fish body was included in the computational domain as a moving wall. The fluid at the interface with the moving boundary was assumed to have the same velocity as the moving wall, giving rise to a one-way coupling from the undulating fish to the surrounding fluid. To capture vorticity generation by the fish body and vortex shedding at the tail, we applied no-slip wall condition at the fish body surface.

The incompressible Navier-Stokes equations were solved numerically using the finite volume method by the commercial software COMSOL Multiphysics (version 5.6). The fluid domain was discretized by a triangular mesh, with five layers of rectangular boundary layer meshes applied at the fish body and the side walls. To account for the time varying fluid domain arising from the oscillatory fish body movements, we employed a deformable mesh to discretize

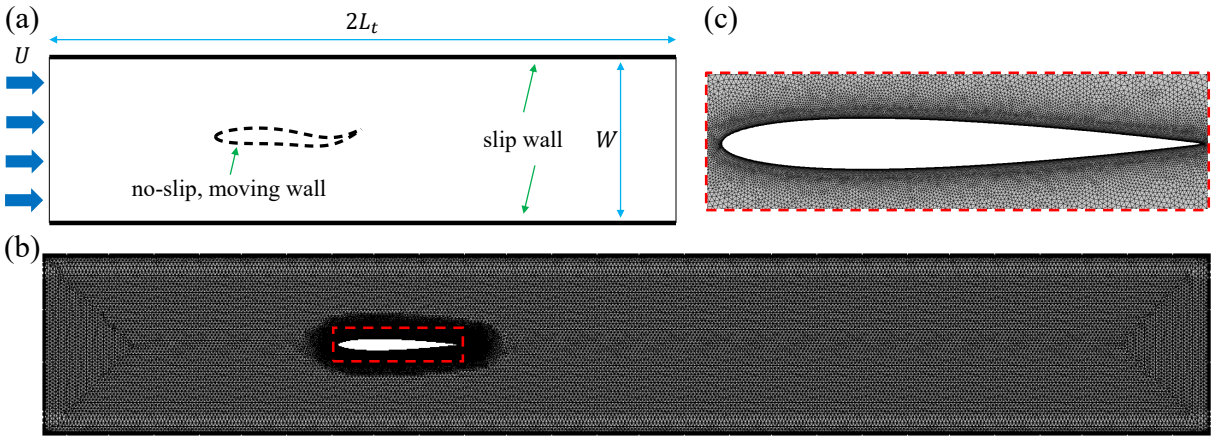

Figure 2: (a) Computational domain with boundary conditions. (b) Mesh generated for CFD analysis of 173k elements, with (c) a zoomed-in view around the fish.

Table 2
Convergence of the maximum drag magnitude on the fish body (per unit depth of the water channel) for nine levels of mesh resolutions.

# elements	23250	33906	72588	87334	108846	122980	148702	172916	204992
max $\lvert F_D \rvert$ (mN/m)	19.87	19.69	19.54	19.52	19.46	19.44	19.40	19.38	19.35

the domain. The mesh deformation was compatible with the movements of the boundaries, such that the velocity of the boundary elements at the fish body surface was equal to the velocity of the fish body, while mesh elements at the inlet, outlet, and the side walls were fixed.

The CFD program was run on a high-performance computing (HPC) cluster with Intel(R) Xeon(R) Platinum 8268 CPUs at a base frequency of 2.90 GHz. Twelve CPUs, with a total memory of 48 GB, were allocated for each computation. A relative tolerance of 1.5×10^{-4} was employed as the convergence criterion at each time step. A typical simulation required a computational time between 12 h and 24 h.

Each simulation was run for 25 tail beating cycles, equivalent to approximately 2.8 s, where the flow in the domain appeared fully developed after approximately five tail beating cycles. We conducted a grid convergence study to identify an adequate computational mesh to accurately capture the flow physics. The mesh was progressively refined, and a new simulation was conducted at each mesh level. To assess convergence, we computed the maximum drag magnitude on the body over the final ten tail beating cycles of each simulation. We observed that a mesh with about 10^5 elements was sufficient for the solution to be mesh independent, whereby further mesh refinements would produce a negligible difference in the hydrodynamic drag, less than 0.05 mN/m (see Figs. 2(b) and 2(c) and Table 2); as such, we performed our simulations with a grid with 173k elements.

2.3. Estimation of the swimming speed

In this study, we focused on steady swimming where the thrust produced by the fish balanced the hydrodynamic drag it experiences. For carangiform swimming, thrust is produced by the cyclic beating of the posterior region of the fish body, while the hydrodynamic drag is experienced dominantly in the anterior part of the body (Ming, Jin, Song, Luo, Du and Ding, 2019). In our simulation, we implemented a swimming pattern with a pre-determined tail beat amplitude and frequency. Consequently, we expected thrust to be marginally influenced by flow speed.

On the other hand, the magnitude of the hydrodynamic drag should depend on the flow speed. Although the latter was available from the experiments (Mwaffo et al., 2017), its value might not accurately satisfy a balance between thrust and drag due to measurement uncertainties and the well-known implications of a two-dimensional simulation environment (Hemelrijk et al., 2015). Hence, we employed an alternative approach, where the flow speed was considered unknown and was determined through a set of additional simulations. Specifically, the flow speed was systematically varied, and the hydrodynamic drag was estimated by integrating the force experienced by the fish along

the swimming direction, $F_D(t)$ (see Fig. 3(a)), over time to compute the average drag, $\bar{F}_D$. The true value of U was inferred by setting $\bar{F}_D = 0$, as illustrated in Fig. 3(b).

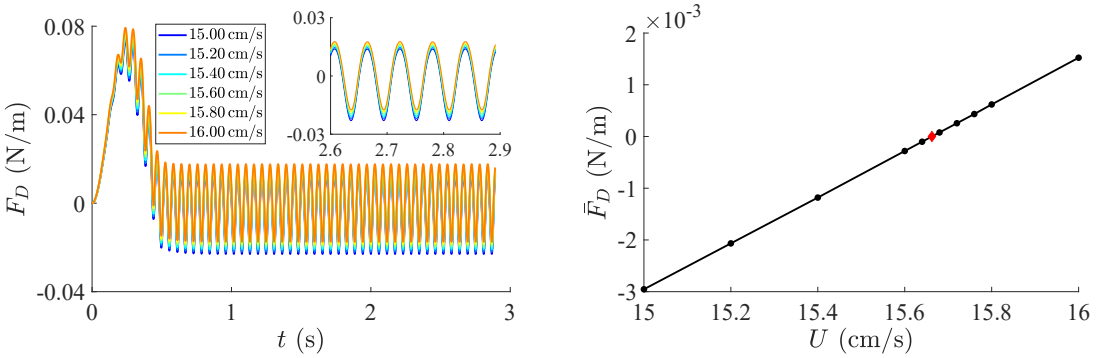

Figure 3: (a) Time histories of the hydrodynamic drag over 25 tail beating cycles for a series of test flow speeds. The inset displays a zoomed-in view of the last five tail beating cycles. (b) The average hydrodynamic drag as a function of the swimming speed. The red diamond on the curve corresponds to $\bar{F}_D = 0$, from which the true value of U was determined.

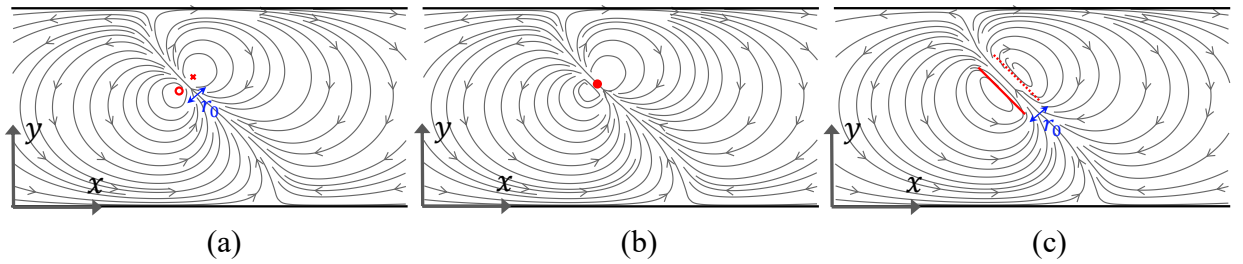

Figure 4: Illustration of the flow streamlines around a (a) finite-dipole, (b) point-dipole, and (c) pair of vortex sheets. In (a), red symbols ∘ and × represent location of the vortices with positive and negative circulation in the dipole, respectively. In (b), the red dot denotes the location of the point-dipole. In (c), the solid red line segment represents a vortex sheet with positive circulation density, and the dotted red line segment represents a vortex sheet with negative circulation density. The separation distances between the pair of vortices in (a) and between the two vortex sheets in (c) are equal to r_0.

3.1. Dipole-based models

The finite-dipole paradigm proposed by Tchieu et al. (2012) contains two point vortices with equal and opposite circulation separated by a fixed distance r_0. The velocity field associated with a finite-dipole in free space could be retrieved from Tchieu et al. (2012) and Kanso and Tsang (2014), among several papers. To account for the presence of the walls, we first quantified the velocity field associated with one vortex positioned between the walls. Specifically, a vortex located at $\boldsymbol{x}_+ = (x_+, y_+)$ between two horizontal walls at $y = 0$ and $y = W$ with a circulation Γ (see Fig. 4(a)) induces a velocity field with components given by

$$u_+(\boldsymbol{x}) = -\frac{\Gamma}{4\pi}\left[\frac{k\sin\left(k\left(y-y_+\right)\right)}{\cosh\left(k\left(x-x_+\right)\right)-\cos\left(k\left(y-y_+\right)\right)} - \frac{k\sin\left(k\left(y-y_+^{\mathrm{im}}\right)\right)}{\cosh\left(k\left(x-x_+\right)\right)-\cos\left(k\left(y-y_+^{\mathrm{im}}\right)\right)}\right], \tag{2a}$$

$$v_+(\boldsymbol{x}) = \frac{\Gamma}{4\pi}\left[\frac{k\sin\left(k\left(x-x_+\right)\right)}{\cosh\left(k\left(x-x_+\right)\right)-\cos\left(k\left(y-y_+\right)\right)} - \frac{k\sin\left(k\left(x-x_+\right)\right)}{\cosh\left(k\left(x-x_+\right)\right)-\cos\left(k\left(y-y_+^{\mathrm{im}}\right)\right)}\right], \tag{2b}$$

where $k = \pi/W$. Equation (2) was derived by the method of images (Newton, 2011), such that the velocity field is the linear superposition of the velocity induced by the vortex and its infinitely many images with respect to the walls. In Eq. (2), y_+^{im} represents the y-coordinate of one of the vortex's images.

Similarly, the velocity field induced by a vortex at $\boldsymbol{x}_- = (x_-, y_-)$ with circulation $-\Gamma$ can be obtained by replacing x_+, y_+, y_+^{im}, and Γ in Eq. (2) with x_-, y_-, y_-^{im}, and $-\Gamma$, respectively. The total velocity associated with the finite-dipole is the superposition of the velocity induced by the positive and negative vortices, that is,

$$\begin{aligned} u(\boldsymbol{x}) = &-\frac{\Gamma}{4\pi}\left[\frac{k\sin\left(k\left(y-y_+\right)\right)}{\cosh\left(k\left(x-x_+\right)\right)-\cos\left(k\left(y-y_+\right)\right)} - \frac{k\sin\left(k\left(y+y_+\right)\right)}{\cosh\left(k\left(x-x_+\right)\right)-\cos\left(k\left(y+y_+\right)\right)}\right] \\ &+\frac{\Gamma}{4\pi}\left[\frac{k\sin\left(k\left(y-y_-\right)\right)}{\cosh\left(k\left(x-x_-\right)\right)-\cos\left(k\left(y-y_-\right)\right)} - \frac{k\sin\left(k\left(y+y_-\right)\right)}{\cosh\left(k\left(x-x_-\right)\right)-\cos\left(k\left(y+y_-\right)\right)}\right], \end{aligned} \tag{3a}$$

$$\begin{aligned} v(\boldsymbol{x}) = &\frac{\Gamma}{4\pi}\left[\frac{k\sin\left(k\left(x-x_+\right)\right)}{\cosh\left(k\left(x-x_+\right)\right)-\cos\left(k\left(y-y_+\right)\right)} - \frac{k\sin\left(k\left(x-x_+\right)\right)}{\cosh\left(k\left(x-x_+\right)\right)-\cos\left(k\left(y+y_+\right)\right)}\right] \\ &-\frac{\Gamma}{4\pi}\left[\frac{k\sin\left(k\left(x-x_-\right)\right)}{\cosh\left(k\left(x-x_-\right)\right)-\cos\left(k\left(y-y_-\right)\right)} - \frac{k\sin\left(k\left(x-x_-\right)\right)}{\cosh\left(k\left(x-x_-\right)\right)-\cos\left(k\left(y+y_-\right)\right)}\right], \end{aligned} \tag{3b}$$

where we have chosen $y_+^{\mathrm{im}} = -y_+$ and $y_-^{\mathrm{im}} = -y_-$.

We denote the mid-point between the two vortices of the dipole as $\boldsymbol{x}_0$ and introduce the two orthogonal unit vectors, $\boldsymbol{e}_0$ and $\boldsymbol{e}_0^{\perp}$, where $\boldsymbol{e}_0$ identifies the direction perpendicular to the line connecting the two vortices and $\boldsymbol{e}_0^{\perp} = \boldsymbol{k}\times\boldsymbol{e}_0$, with $\boldsymbol{k}$ being the out-of-plane unit vector. Using this notation, we can express $\boldsymbol{x}_+ = \boldsymbol{x}_0 + \frac{1}{2}r_0\boldsymbol{e}_0^{\perp}$ and $\boldsymbol{x}_- = \boldsymbol{x}_0 - \frac{1}{2}r_0\boldsymbol{e}_0^{\perp}$.

For two freely advecting vortices in a channel, their separation distance r_0 could vary over time. In contrast, within the finite-dipole paradigm, this distance is enforced to be constant such that the two vortices do not collapse into or split from each other. Such a constant value for the separation distance requires an internal inter-vortex forcing that constraints the relative speed of the vortices to zero (Tchieu et al., 2012; Kanso and Tsang, 2014).

The finite-dipole elicits a self-induced velocity, which can be estimated as the mean advective velocity of both vortices in the dipole. For the vortex located at $\boldsymbol{x}_+$, its advective velocity can be obtained by taking the limit of $\boldsymbol{x}\to\boldsymbol{x}_+$ in Eq. (3), which gives rise to a singularity in the form of

$$\left(-\frac{\Gamma}{2\pi}\frac{y-y_+}{r^2}, \frac{\Gamma}{2\pi}\frac{x-x_+}{r^2}\right), \quad \text{as } r\to 0, \tag{4}$$

where $r = |\boldsymbol{x}-\boldsymbol{x}_+|$. In the estimation of the advective velocity, the singularity in Eq. (4) should be subtracted from Eq. (2) before evaluating the limit for $\boldsymbol{x}\to\boldsymbol{x}_+$. The advective, self-induced, velocity is determined as

$$\begin{aligned} u_+^{\mathrm{s}}(\boldsymbol{x}) = &\frac{\Gamma}{4\pi}\frac{k\sin\left(2ky_+\right)}{1-\cos\left(2ky_+\right)} + \frac{\Gamma}{4\pi}\left[\frac{k\sin\left(k\left(y_+-y_-\right)\right)}{\cosh\left(k\left(x_+-x_-\right)\right)-\cos\left(k\left(y_+-y_-\right)\right)}\right. \\ &\left. - \frac{k\sin\left(k\left(y_++y_-\right)\right)}{\cosh\left(k\left(x_+-x_-\right)\right)-\cos\left(k\left(y_++y_-\right)\right)}\right], \end{aligned} \tag{5a}$$

$$v_+^{\mathrm{s}}(\boldsymbol{x}) = -\frac{\Gamma}{4\pi}\left[\frac{k\sin\left(k\left(x_+-x_-\right)\right)}{\cosh\left(k\left(x_+-x_-\right)\right)-\cos\left(k\left(y_+-y_-\right)\right)} - \frac{k\sin\left(k\left(x_+-x_-\right)\right)}{\cosh\left(k\left(x_+-x_-\right)\right)-\cos\left(k\left(y_++y_-\right)\right)}\right]. \tag{5b}$$

We notice from Eq. (5) that for a single point vortex in the channel, its interaction with the walls leads to a non-zero velocity parallel to the wall at the location of the vortex (Newton, 2011). This is different from a single point vortex in free space, where its self-induced velocity would be zero.

Expressions for the advective velocity of the other vortex, $\boldsymbol{u}_-^{\mathrm{s}}$, is equivalent to Eq. (5). The self-induced velocity of the finite-dipole can then be estimated as $\boldsymbol{u}_0^{\mathrm{s}} = \frac{1}{2}\left(\boldsymbol{u}_+^{\mathrm{s}} + \boldsymbol{u}_-^{\mathrm{s}}\right)$. As evidenced from Eq. (5), the magnitude of the

self-induced velocity depends on the inter-vortex distance r_0, the magnitude of circulation Γ, and the proximity to the wall.

In the limiting case where the distance between the two vortices becomes infinitesimally small, $r_0 \to 0$, the finite-dipole system converges to a point-dipole, whose velocity field between two horizontal walls (see Fig. 4(b)) has been derived in Porfiri et al. (2022). Assuming that the dipole maintains the self-induced advective velocity $\boldsymbol{u}_0^{\mathrm{s}} = v_0 \boldsymbol{e}_0$ and orientation $\boldsymbol{e}_0$, the velocity field as $r_0 \to 0$ can be decomposed as

$$u(\boldsymbol{x}) = u^{\mathrm{fs}}(\boldsymbol{x}) + u^{\mathrm{w}}(\boldsymbol{x}), \tag{6a}$$

$$v(\boldsymbol{x}) = v^{\mathrm{fs}}(\boldsymbol{x}) + v^{\mathrm{w}}(\boldsymbol{x}), \tag{6b}$$

where we identify the velocity in free space $\boldsymbol{u}^{\mathrm{fs}}(\boldsymbol{x})$ and the velocity due to the presence of the walls $\boldsymbol{u}^{\mathrm{w}}(\boldsymbol{x})$. The free space velocity reads

$$u^{\mathrm{fs}}(\boldsymbol{x}) = \hat{r}_0^2 v_0 \frac{((x-x_0)^2-(y-y_0)^2)\cos\theta + 2(x-x_0)(y-y_0)\sin\theta}{((x-x_0)^2+(y-y_0)^2)^2}, \tag{7a}$$

$$v^{\mathrm{fs}}(\boldsymbol{x}) = \hat{r}_0^2 v_0 \frac{-((x-x_0)^2-(y-y_0)^2)\sin\theta + 2(x-x_0)(y-y_0)\cos\theta}{((x-x_0)^2+(y-y_0)^2)^2}, \tag{7b}$$

where θ is the angle between $\boldsymbol{e}_0$ and the x-axis. The wall-induced velocity can be expressed as

$$\begin{aligned} u^{\mathrm{w}}(\boldsymbol{x}) =& \frac{\hat{r}_0^2 v_0}{4}\left[\frac{\pi^2 e^{-i\theta}}{2W^2}\left(e^{2i\theta}\left(\operatorname{csch}^2\pi A + \operatorname{csch}^2\pi B^*\right) + \operatorname{csch}^2\pi A^* + \operatorname{csch}^2\pi B\right)\right. \\ &\left. + \frac{4\cos\theta}{(x-x_0)^2+(y-y_0)^2} - \frac{8(x-x_0)((x-x_0)\cos\theta_f + (y-y_0)\sin\theta)}{((x-x_0)^2+(y-y_0)^2)^2}\right], \end{aligned} \tag{8a}$$

$$\begin{aligned} v^{\mathrm{w}}(\boldsymbol{x}) =& \frac{\hat{r}_0^2 v_0}{4}\left[\frac{i\pi^2 e^{-i\theta}}{2W^2}\left(e^{2i\theta}\left(\operatorname{csch}^2\pi A - \operatorname{csch}^2\pi B^*\right) - \operatorname{csch}^2\pi A^* + \operatorname{csch}^2\pi B\right)\right. \\ &\left. + \frac{4\sin\theta}{(x-x_0)^2+(y-y_0)^2} - \frac{8(y-y_0)((x-x_0)\cos\theta + (y-y_0)\sin\theta)}{((x-x_0)^2+(y-y_0)^2)^2}\right], \end{aligned} \tag{8b}$$

where $A = ((x-x_0)+i(y-y_0))/(2W)$, $B = ((x-x_0)+i(y+y_0))/(2W)$, $i = \sqrt{-1}$ is the imaginary unit, and $(\cdot)^*$ indicates complex conjugate. In Eqs. (7) and (8), we retained a characteristic length scale $\hat{r}_0$ associated with the amplitude of a fish tail beat, which is related to the circulation of one vortex in the dipole through

$$\Gamma = 2\pi \hat{r}_0 v_0. \tag{9}$$

3.2. Vortex sheet-based model

The dipole-based models described in Sec. 3.1 can provide meaningful insight into the flow in the far-field, upon which we have recently studied the rheotactic behavior of a fish swimming in a channel (Porfiri et al., 2022) and the emergence of in-line swimming in fish pairs (Porfiri et al., 2021). While dipole-based models can successfully reproduce the flow pattern from the fish head to the tail, they cannot capture the elongated streamlines along the fish body, which are often observed experimentally (Windsor et al., 2010a,b), due to its slender shape. This discrepancy might challenge the validity of near-body interactions, such as coordinated swimming of individuals closely packed in a school or swimming near walls.

A feasible approach to address this issue is a model based on vortex sheets, defined as imaginary surfaces in three-dimensions (lines in two-dimensions) across which the tangential flow velocity is discontinuous (Saffman, 1993). For a pair of parallel, flat vortex sheets ($\mathcal{C}_+$ and $\mathcal{C}_-$) separated by a fixed distance r_0, the flow field features streamlines connecting one end of the vortex sheet pair to the other, qualitatively similar to the flow field around a finite-dipole or a point-dipole. Importantly, the pair of vortex sheets could generate elongated streamline patterns (see Fig. 4(c)), resembling those around fish (Kern and Koumoutsakos, 2006).

We assume $\mathcal{C}_+$ to have a circulation density (per unit length) of $\gamma(\boldsymbol{x}_+)$, oriented along the $\boldsymbol{e}_0$ direction. The other vortex sheet, $\mathcal{C}_-$, is taken to be a copy of $\mathcal{C}_+$ with opposite circulation density, translated to the right side of $\mathcal{C}_+$ along

the $-\boldsymbol{e}_0^{\perp}$ direction by a distance r_0 (see Fig. 4(c)). To facilitate the description of the pair of vortex sheets, we define θ as the angle between its orientation $\boldsymbol{e}_0$ with the x-axis, $\mathcal{L}$ as its length, and $\boldsymbol{x}_0$ as the position of the mid-point between the centers of the two sheets. The associated velocity field in the domain between the horizontal walls at $y = 0$ and $y = W$ is

$$\begin{aligned} u(\boldsymbol{x}) = &-\frac{1}{4\pi}\int_{C_+}\gamma(\boldsymbol{x}_+)\left[\frac{k\sin\left(k\left(y-y_+\right)\right)}{\cosh\left(k\left(x-x_+\right)\right)-\cos\left(k\left(y-y_+\right)\right)}\right.\\ &\left.-\frac{k\sin\left(k\left(y+y_+\right)\right)}{\cosh\left(k\left(x-x_+\right)\right)-\cos\left(k\left(y+y_+\right)\right)}\right]\mathrm{d}\boldsymbol{x}_+\\ &-\frac{1}{4\pi}\int_{C_-}\gamma(\boldsymbol{x}_-)\left[\frac{k\sin\left(k\left(y-y_-\right)\right)}{\cosh\left(k\left(x-x_-\right)\right)-\cos\left(k\left(y-y_-\right)\right)}\right.\\ &\left.-\frac{k\sin\left(k\left(y+y_-\right)\right)}{\cosh\left(k\left(x-x_-\right)\right)-\cos\left(k\left(y+y_-\right)\right)}\right]\mathrm{d}\boldsymbol{x}_-, \end{aligned} \tag{10a}$$

$$\begin{aligned} v(\boldsymbol{x}) = &\frac{1}{4\pi}\int_{C_+}\gamma(\boldsymbol{x}_+)\left[\frac{k\sin\left(k\left(x-x_+\right)\right)}{\cosh\left(k\left(x-x_+\right)\right)-\cos\left(k\left(y-y_+\right)\right)}\right.\\ &\left.-\frac{k\sin\left(k\left(x-x_+\right)\right)}{\cosh\left(k\left(x-x_+\right)\right)-\cos\left(k\left(y+y_+\right)\right)}\right]\mathrm{d}\boldsymbol{x}_+\\ &+\frac{1}{4\pi}\int_{C_-}\gamma(\boldsymbol{x}_-)\left[\frac{k\sin\left(k\left(x-x_-\right)\right)}{\cosh\left(k\left(x-x_-\right)\right)-\cos\left(k\left(y-y_-\right)\right)}\right.\\ &\left.-\frac{k\sin\left(k\left(x-x_-\right)\right)}{\cosh\left(k\left(x-x_-\right)\right)-\cos\left(k\left(y+y_-\right)\right)}\right]\mathrm{d}\boldsymbol{x}_-. \end{aligned} \tag{10b}$$

While the integrals in Eq. (10) are difficult to exactly evaluate for vortex sheets of arbitrary lengths and shapes, the velocity field can be well estimated through numerical integration. Briefly, sheets C_+ and C_- are discretized into elements with equal length Δs, which are treated as individual point vortices with circulation $\gamma(\boldsymbol{x}_+)\Delta s$ and $\gamma(\boldsymbol{x}_-)\Delta s$, respectively. Integrals in Eq. (10) are then approximated by a linear superposition of the velocity field induced by each element, equivalent to the quantification of the velocity field associated with an array of discrete point vortices (Aref and Siggia, 1981). Similar numerical techniques have been successfully implemented for the investigation of vortical structures generated in the wake of a fish (Wolfgang, Anderson, Grosenbaugh, Yue and Triantafyllou, 1999), formation of vortex rings (Nitsche and Krasny, 1994), and Kelvin-Helmholtz instability of a shear flow (Ashurst and Meiburg, 1988).

The advective velocity of any point of a sheet $\boldsymbol{x}_s$ ($\boldsymbol{x}_s \in C_+ \cup C_-$) can be obtained by taking the limit $\boldsymbol{x} \to \boldsymbol{x}_s$ in Eq. (10). Similar to a finite-dipole, a singularity in the velocity emerges as $\boldsymbol{x} \to \boldsymbol{x}_s$, which can be treated by subtracting the expression in (4) from the integrands in Eq. (10). An alternative approach to de-singularize is to add a small, positive value, $\frac{1}{2}k^2\delta^2$, to the denominator of the first term of each integrand in Eq. (10). Here, δ is a small value on the order of the inter-vortex distance, thereby eliminating the singularity in Eq. (10). This approach is equivalent to treating a vortex sheet as an array of vortices with a finite core size determined by δ, which would lead to a smooth velocity field across the sheet Ashurst and Meiburg (1988). From preliminary tests, we discovered that the two approaches for de-singularization produced equivalent advective sheet velocities and velocity fields in the channel with negligible differences. In the current implementation, we consistently adopted the latter approach owing to its ease of numerical implementation.

In general, different segments of a free vortex sheet could advect at different velocities Higdon and Pozrikidis (1985), which may lead to the stretching and rolling of the sheet similar to Ashurst and Meiburg (1988). To ensure that the vortex sheets do not deform and the inter-sheet distance does not vary over time, we assumed an internal inter-vortex forcing, such that in the discretized sheet model the distance between any pair of vortices is fixed over time. This internal forcing is similar to the one introduced in the finite-dipole by Tchieu et al.Tchieu et al. (2012) to maintain a constant inter-vortex distance.

3.3. Identification of model parameters

Physical parameters in the dipole- and vortex sheet-based models were determined by fitting their predicted velocity fields to the numerical results obtained in Sec. 2.2. Specifically, for the velocity associated with the point-dipole in Eq. (6), we considered the dipole location, $\boldsymbol{x}_0$, and the characteristic length, $\hat{r}_0$, as fitting parameters, while setting υ_0 to be equal to the fish swimming speed. We expected $\boldsymbol{x}_0$ to be correlated to the location of the fish, while $\hat{r}_0$ to indirectly determine the circulation strength through Eq. (9). Similarly, in Eq. (3), we treated the location of the finite-dipole, $\boldsymbol{x}_0$, and the separation distance between the vortices, r_0, as the fitting parameters. The value of Γ in Eq. (3) was indirectly determined by matching the advective speed of the dipole with the swimming speed of the fish. For the velocity associated with a pair of vortex sheets in Eq. (10), we regarded the center of the sheet $\left(\boldsymbol{x}_0\right)$, the separation distance between sheets $\left(r_0\right)$, and the sheet length ($\mathcal{L}$) as fitting parameters. To ease implementation of the model in practical settings, we chose the circulation densities of the sheets to be constant, $\gamma(\boldsymbol{x}_\pm) = \pm\gamma$; the value of γ was selected such that the mean velocity of the sheet matched the swimming velocity of fish. The performance of vortex sheets with nonuniform circulation density for the prediction of the flow field is explored in Appendix A.

Consistent with the fish configuration depicted in Fig. 2, in the dipole- and vortex sheet-based models, we set the orientation angle to be $\theta = \pi$, and the vertical location at $y_0 = W/2$, such that a dipole or the pair of vortex sheets was positioned at the center of the channel orienting upstream.

The discrepancy between the modeled velocity field $\left(\boldsymbol{u}^{\text{model}}\right)$ and the numerical results $\left(\boldsymbol{u}^{\text{CFD}}\right)$ was quantified by a function, $\Delta\boldsymbol{u}$, defined as

$$\Delta\boldsymbol{u} = \boldsymbol{u}^{\text{CFD}} - \boldsymbol{u}^{\text{model}}, \tag{11}$$

where $\boldsymbol{u}^{\text{CFD}}$ is the mean velocity field over the final ten tail beat cycles in numerical simulations relative to the background flow. The quality of the fitting was evaluated through an error metric,

$$E = \sqrt{\frac{\int_{\mathcal{D}} |\Delta\boldsymbol{u}|^2 \, \mathrm{d}S}{\int_{\mathcal{D}} \mathrm{d}S}}, \tag{12}$$

where $\mathcal{D}$ is the computational domain illustrated in Fig. 2(a).

The optimal fitting parameters for each model considered in Secs. 3.1 and 3.2 were determined through an exhaustive search within a predefined search space. To ensure adequate efficiency of the exhaustive search, we adopted a multi-step approach, where an initial search was conducted on a large parameter space with a grid that equally discretized each parameter. The separation distance (r_0 or $\hat{r}_0$) spanned between zero and twice the tail beating amplitude of fish. For dipole-based models, the location of the dipole $\left(\boldsymbol{x}_0\right)$ varied between 20% in front of and 20% in the wake of the fish. For the vortex sheet-based model, the location of the sheets $\left(\boldsymbol{x}_0\right)$ was such that the left end of the sheets varied between 20% in front of and 20% behind the fish head. The length of the sheets was varied between zero and $1.5L$. Following the initial search, we conducted another search within a reduced domain near the global minimum on a refined grid. This process was repeated three times, resulting in a set of optimal fitting parameters corresponding to the minimum value of E. For the search space considered here, typical values of E/U ranged between 3% and 70%.

3.4. Further validation of the vortex sheet-based model

Upon comparing the dipole- and vortex sheet-based models with numerical results, we conducted an in-depth analysis of the accuracy of the vortex sheet-based model. To this end, we systematically varied the fish swimming speed and the width of the channel, and we quantified the accuracy of the vortex sheet-based model in predicting the mean flow field around the fish.

Specifically, we varied the inlet flow speed in CFD simulations between 5 cm/s and 50 cm/s. At each swimming speed, we adjusted the body undulation frequency, f, accordingly, such that force equilibrium between the mean hydrodynamic drag and propulsion was satisfied. Following the procedure outlined in Sec. 2.2, we obtained the mean velocity field around the swimming fish. The parameters of the vortex sheet-based model was calibrated for each swimming speed, and model accuracy was evaluated in terms of the error defined in Eq. (12).

We then investigated the effect of the channel width on the accuracy of the vortex sheet-based model by systematically varying the width of the computational domain. The same locomotory patterns detailed in Sec. 2.1 were employed in all simulations. We varied the width of the swimming domain W from 3 cm to 15 cm in CFD simulations, and adjusted the inlet flow speed accordingly such that the equilibrium between the mean hydrodynamic drag and propulsion was maintained. The velocity field for each channel width was fitted using the vortex sheet-based model, and results were compared using the error metric in Eq. (12).

4. Results

4.1. CI

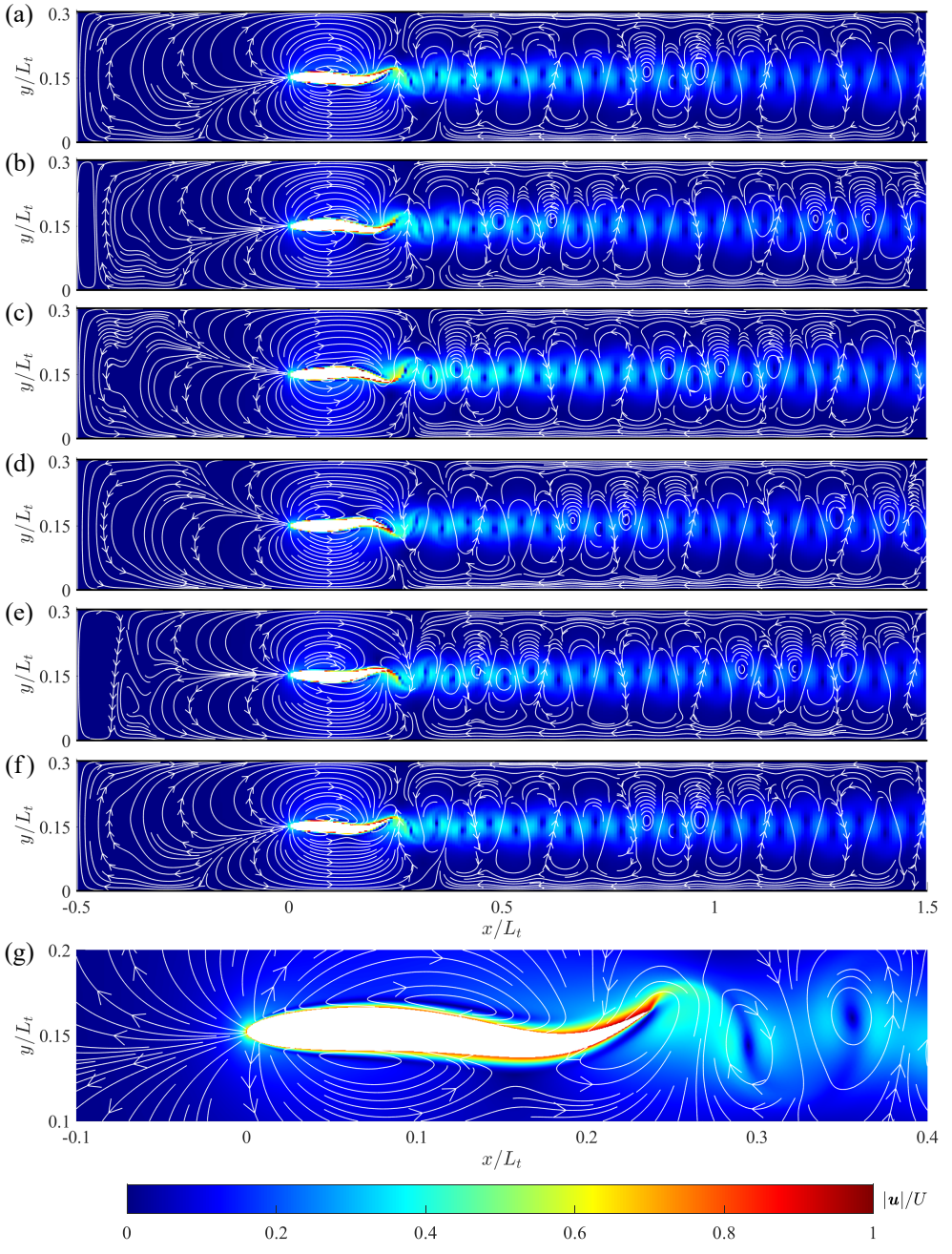

Figure 5: Flow fields around a swimming fish relative to the background flow; (a)-(f) identify consecutive snapshots of the velocity field over one tail beat cycle. A zoom-in view of the flow field around the fish body in (f) is shown in (g). White curves and arrows represent velocity streamlines and velocity directions.

In Fig. 5, we display the instantaneous flow fields around the fish at a few time instances over one tail beat cycle during steady swimming. Here, we have subtracted the background flow from the instantaneous flow fields to emphasize the flow generated by the fish. Two main features can be noticed in the flow field around the swimming fish. In the vicinity of the body, the instantaneous velocity field contains a flow circulation from the head to tail, as evidenced

by the velocity streamlines in Fig. 5. A clockwise circulation is observed on the right side of the body, while a counter-clockwise circulation is registered on the left side. This instantaneous flow circulation is asymmetric about the centerline of the computational domain. The asymmetry in the flow streamlines is magnified in the upstream, causing a marginal cross-channel flow that switches its direction over a tail beating cycles.

The other marked feature of the instantaneous flow fields is the unsteady wake, containing a downstream flow with transverse velocity components in alternating directions. The wake originates from the formation of the thin boundary layers along the body surface. The flow developed in the boundary layer is ultimately shed into the wake by the undulatory movements of the fish tail. The magnitude of the wake flow remains strong within one body length, and it decays as it is advected downstream. This flow pattern in the wake was described by Wu (2011) as a "locomotive vortex street", which was associated with thrust generation.

To compare CFD results with dipole- and vortex sheet-based models, we examine the mean flow field over the final ten tail beat cycles, as displayed in Fig. 6(a). The main features observed in the instantaneous flow are retained in the time-averaged flow field around the fish. The near-body flow becomes symmetric with respect to the centerline of the fish body, while an axial elongation of the streamlines along the body is evident. In the wake, the transverse flow generated by fish tail beating is reduced as a result of time-averaging. The resulting wake flow contains a downstream jet with a considerably lower velocity magnitude compared with the near-body circulatory flow.

4.2. Comparison between predictions of CFD and mathematical models

The accuracy of dipole- and vortex sheet-based models is assessed through direct comparison of the analytical models with CFD simulations. For each model described in Sec. 3, we identify a set of optimal fitting parameters defined in Sec. 3.3, such that the error in Eq. (12) between the model predicted and the numerically quantified flow fields is minimized. The velocity fields predicted by a point-dipole, a finite-dipole, and a pair of vortex sheets, along with their discrepancy with the numerical results, $|\Delta \boldsymbol{u}|$, are displayed in Fig. 6.

The optimal locations of both the point-dipole and the finite-dipole are at approximately a quarter body length from the fish head long the centerline. As shown in Figs. 6(b) and (d), the velocity fields predicted by the point-dipole and the finite-dipole capture the main recirculating flow patterns on both sides of the fish body. The streamlines remain nearly circular near the body, and they appear to be elongated horizontally only in close proximity to the walls as a result of the no-penetration boundary condition.

Despite their agreement with numerical results in Fig. 6(a), we identify a major inaccuracy in the flow field predicted by the dipole-based models. On the sides of the fish body, both the point-dipole and the finite-dipole fail to capture the elongated shape of the streamline patterns. This can be further attested by the difference between model predictions and numerical simulations, $|\Delta \boldsymbol{u}|$, where a substantial discrepancy is evident near the head and tail for both the point-dipole and the finite-dipole, as shown in Figs. 6(c) and (e), respectively.

The equivalent performance of the two dipole-based models is also reflected in the marginal difference between their errors estimated through Eq. (12). We report a relative error of $E/U = 4.35\%$ and $E/U = 4.42\%$ for the point-dipole and the finite-dipole, respectively. Although the finite-dipole model allows us to tune the distance between the two point vortices, it does not lead to an appreciably improved accuracy in the prediction of the flow field compared with the point-dipole model.

The velocity field predicted by the proposed vortex sheet-based model is presented in Fig. 6(f). The fitted pair of vortex sheets cover 81% of the body length, and the location of the mid-point was such that the vortex sheets run from the head of the fish, leaving only 1.5% of the frontal region uncovered. The separation between the two vortex sheets is approximately 46% of the body width. As evidenced in Fig. 6(f), not only does the pair of vortex sheets succeed in capturing the flow patterns from the head to the tail, but it also produces an elongated streamline pattern that is remarkably similar to numerical findings. Only a marginal discrepancy between model predictions and numerical simulations of the velocity field is registered in a thin fluid layer enclosing the body, as illustrated in Fig. 6(g). This is likely due to a boundary layer flow developed at the body surface, which could not be captured by the vortex sheet-based model as a result of its inviscid assumption. The superior performance of the vortex sheet-based model is further corroborated by its lower error of $E/U = 3.16\%$, approximately a 28% reduction compared with dipole-based models.

In addition to the major discrepancy noted in the near-field, we registered a secondary inaccuracy in the prediction of the flow in the wake, as illustrated by the moderate error in the wake flows in Figs. 6(c), (e), and (f). In principle, the wake flow can potentially be captured by superimposing free vortex sheets to these models (Wu, 2011). Formulation

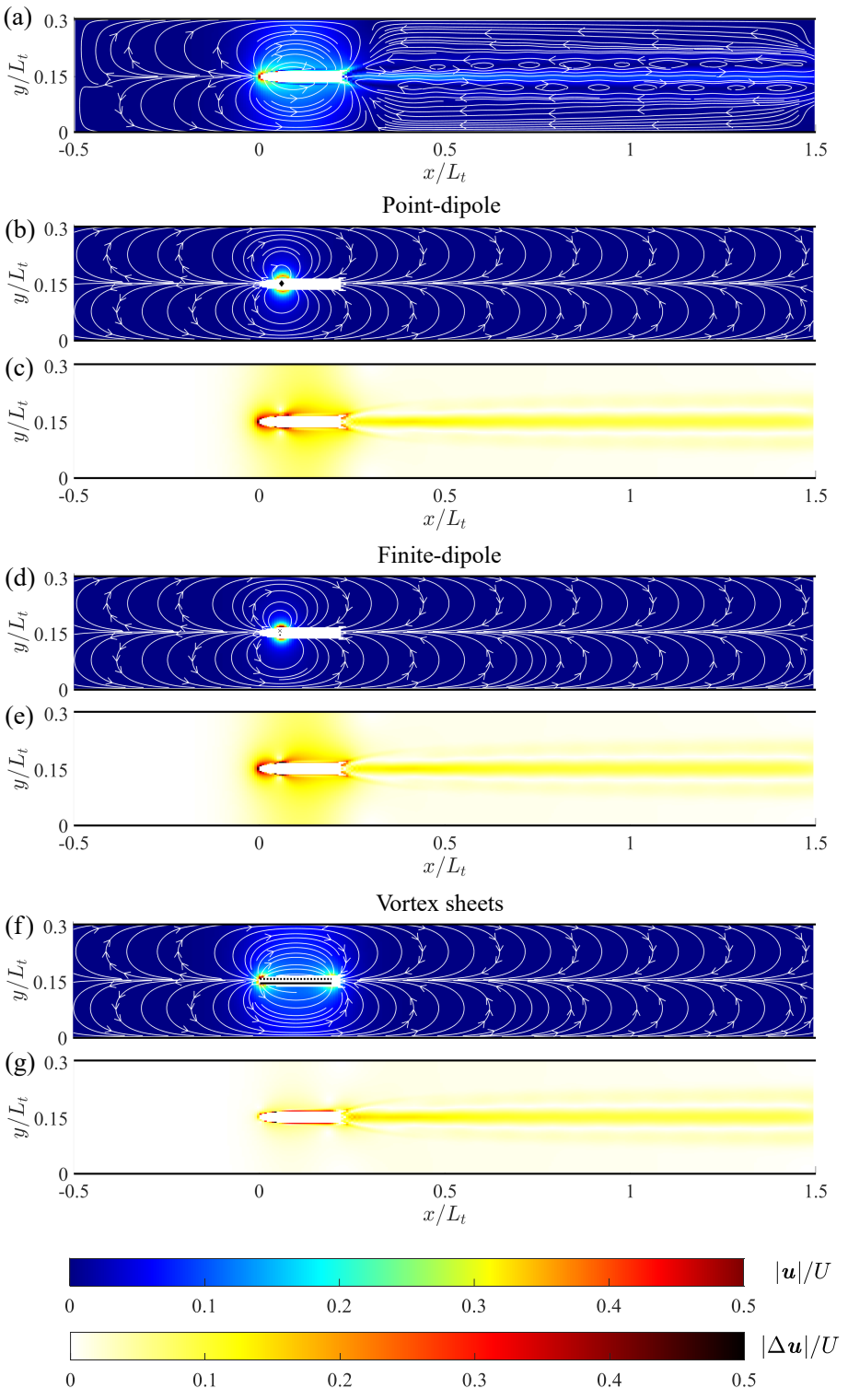

Figure 6: (a) Mean flow field around the swimming fish relative to the background flow, quantified through CFD. Velocity fields predicted by the point-dipole, the finite-dipole, and the vortex sheet-based models in the absence of a background flow are displayed in (b), (d), and (f), respectively. Discrepancy between CFD results and predictions of point-dipole, the finite-dipole, and the vortex sheet-based models are shown in (c), (e), and (g), respectively. In (a), (b), (d), and (f), color represents the velocity magnitude scaled by the swimming speed, $|\boldsymbol{u}|/U$, and white curves and arrows represent velocity streamlines and directions. In (c), (e), and (g), color represents magnitude of error scaled by the swimming speed, $|\Delta\boldsymbol{u}|/U$.

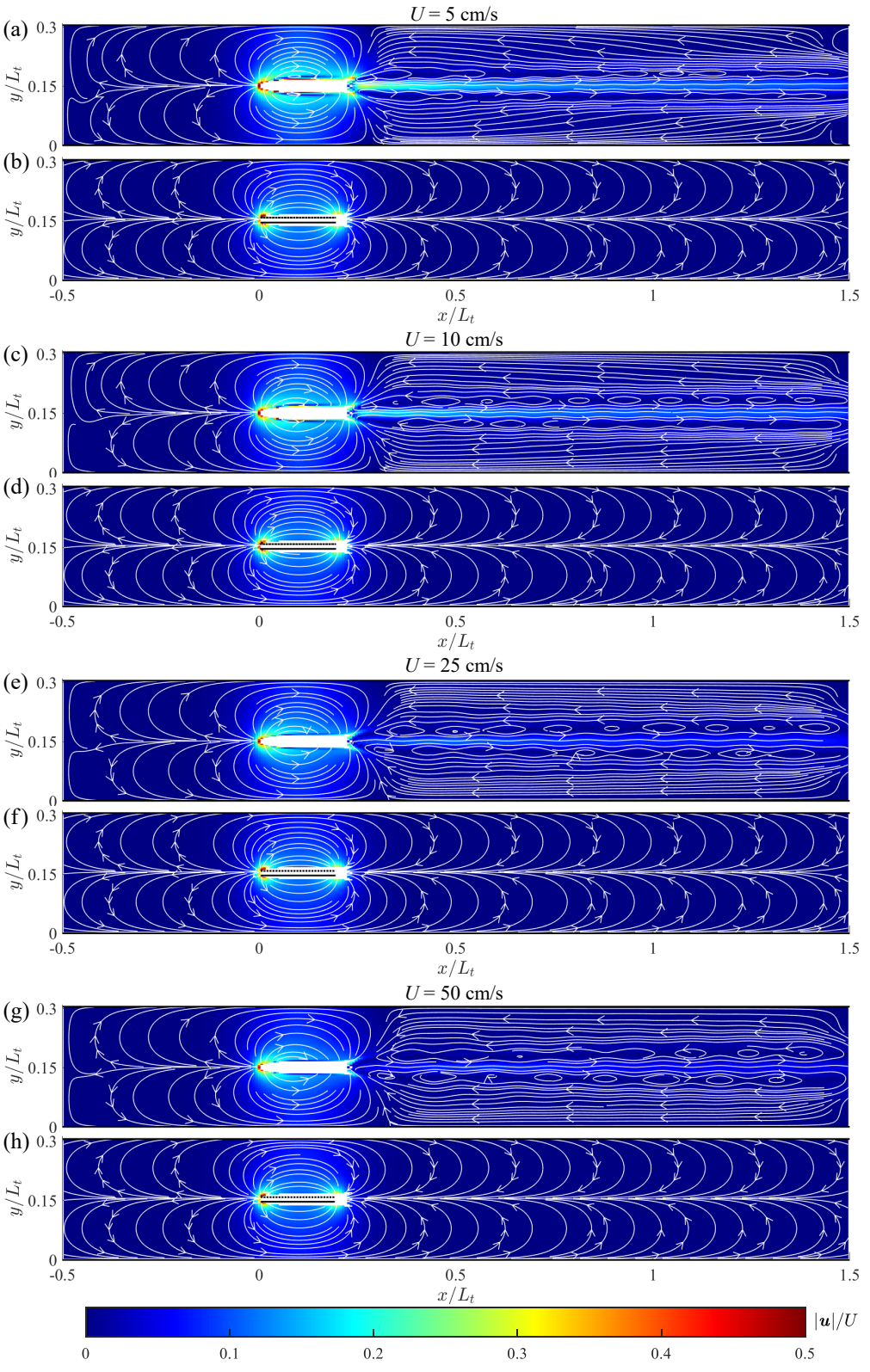

Figure 7: Computational results of the mean flow fields around the fish swimming at speed (a) $U = 5\,\mathrm{cm/s}$, (c) $U = 10\,\mathrm{cm/s}$, (e) $U = 25\,\mathrm{cm/s}$, and (g) $U = 50\,\mathrm{cm/s}$, relative to the background flow. The corresponding velocity fields fitted by the vortex sheet-based model are displayed in (b), (d), (f), and (h), respectively. Color represents the velocity magnitude scaled by the corresponding swimming speed, $|\boldsymbol{u}|/U$, and white curves and arrows represent velocity streamlines and directions.

and validation of such a generalized model is beyond the scope of the present study and will be investigated in a future work, outlined in the concluding section (Sec. 5).

The accuracy in predicting the velocity field around the swimming fish could be, in principle, improved by vortex sheets with nonuniform circulation density. To test this possibility, in Appendix A, we present predictions of the velocity field by nonuniform vortex sheets and the associated error. Our analysis indicates that nonuniform vortex sheets leads to an error of $E/U = 3.07\%$, which is only a marginal improvement in accuracy compared to uniform vortex sheets (3.16% versus 3.07%). As a result, the assumption of uniform circulation density is retained in the rest of this work for its ease of implementation.

4.3. Sensitivity analysis on the accuracy of the vortex sheet-based model

Building upon the compelling accuracy of the vortex sheet-based models, we evaluated their performance in modeling fish swimming across a wide range of swimming speeds. As shown in Fig. 7(a), (c), (e), and (g), upon scaling by the swimming speed, U, the velocity fields around the swimming fish are remarkably similar among all swimming speeds tested. The main features of the flow, including the head-to-tail flow pattern and the secondary wake flow observed in Fig. 6(a) for $U = 15.66\,\mathrm{cm/s}$, are retained at all swimming speeds. Two major variations are noticed in the flow field at different swimming speeds. First, on the body surface, the thickness of the boundary layer decreases as we increase U, due to the smaller boundary layer thickness associated with larger Reynolds numbers. Second, while at $U \geq 25\,\mathrm{cm/s}$ the wake flow is hardly noticeable (Figs. 7(e) and (g)), a robust downstream jet flow is produced by fish swimming at lower speeds (Figs. 7(a) and (c)). This could be attributed to the enhanced viscous effect in the wake at lower Reynolds numbers, which promotes vorticity production by the tail.

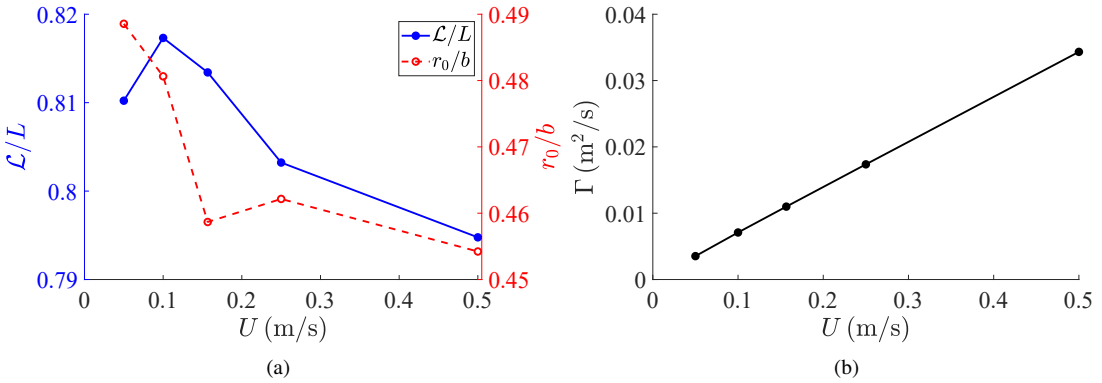

Figure 8: (a)The length and separation distance of the vortex sheets and (b) the magnitude of the total circulation of a vortex sheet in the pair of sheets as a function of the swimming speed.

The flow fields predicted by the vortex sheet-based model agree well with the numerical simulations at all swimming speeds. Consistent with the marginal influence of the velocity field on the swimming speed observed from the numerical results, the optimal fitting parameters of the vortex sheets, including their lengths and separation distances, distribute within a narrow range. Among all swimming speeds tested, the vortex sheets span 79% to 82% of the body length, and their separation distances cover 45% to 49% of the body width (see Fig. 8(a)). The location of the mid-point did not display any significant change, so that the vortex sheet would always begin from the head of the fish. The accuracy of model predictions exhibits a moderate improvement as the swimming speed increases, whereby the relative error, E/U, reduces from 4.68% to 1.99% as U is increased from 5 cm/s to 50 cm/s. In this vein, one could simply modify the circulation and retain the length of the sheets and their separation at 80% of the fish length and 50% of the fish width, respectively. The larger error at lower swimming speed could be attributed to the inadequacy of the potential flow hypothesis to describe boundary layers and wake flow.

For completeness, we also report values of the circulation, Γ, for different speeds. As shown in Fig. 8(b), the magnitude of the total flow circulation generated by a vortex sheet in the pair is linearly proportional to the swimming speed, U. This is consistent with both experimental measurements (Mwaffo et al., 2017) and analytical estimations using the slender-body theory (Vorus and Taravella, 2011), where a higher circulation is required to produce larger

thrust at higher swimming speeds. The linear dependence of Γ on U over the large range of swimming speeds tested is a beneficial characteristic of the vortex sheet-based model, as the circulation identified at one swimming speed can be interpolated to inform the prediction of the velocity field at other speeds.

To further assess the effect of the channel width on the accuracy of the vortex sheet-based model, in Fig. 9, we display the velocity field around the fish in a range of channel widths between $W = 3$ cm and 15 cm (corresponding to channel width-to-body length ratios between $W/L = 0.85$ and 4.23). The width of the channel elicits a negligible influence on the fish swimming speed. In a narrow domain of $W = 3$ cm, the elongation of the streamline pattern is exacerbated by the proximity of the channel walls, as illustrated in Fig. 9(a). The influence of the channel walls becomes negligible as W is increased above 10 cm, where the streamline patterns in the vicinity of the fish body become indistinguishable between $W = 10$ cm and $W = 15$ cm, as shown in Figs. 9(c) and (e).

The vortex sheet-based model is employed to fit the velocity field around the fish for all domain widths. The model is successful in predicting the shapes of the streamlines and the magnitudes of the velocity fields, as evidenced in Figs. 9(b), (d), and (f). The relative error, E/U, reduces from 4.46% to 1.90% as the width W is increased from 3 cm to 15 cm. The optimal fitting parameters of the vortex sheet-based model distribute within a narrow range, where the vortex sheets span 81% to 84% of the body length, their separation distances cover 45% to 47% of the body width, and the magnitude of circulation of one sheet is between $0.0110\,\mathrm{m}^2/\mathrm{s}$ and $0.0113\,\mathrm{m}^2/\mathrm{s}$. No significant change is documented on the location of the mid-point of the vortex sheets. The independence of the fitting parameters from the swimming domain is a favorable feature of the proposed model, whereby calibration of the model based on simulation results of one swimming domain is sufficient to produce an accuracy prediction for the velocity field in a domain of a different size.

5. Discussion and conclusions

In this work, we examined the validity of classical dipole-based models of fish swimming through systematic comparison against numerical results obtained as part of a two-dimensional CFD campaign informed by experimental data. We demonstrated that dipole-based models are capable of capturing the main features of the mean flow around the fish body. The dipole-based models were successful in generating flow patterns from the fish head to the tail, which is in qualitative agreement with the numerical results. However, they are not adequate to explain elongated streamline patterns along the fish length, observed in the simulations.

The discrepancy in the streamline patterns was mitigated by a variation of the dipole-based model, originally proposed in this study. Rather than lumping the entire hydrodynamics in a single vortex pair, the proposed model utilizes two parallel vortex sheets along the fish length. The vortex sheet-based model begets improved accuracy in the prediction of the velocity field with respect to dipole-based models. Importantly, across a wide range of simulation studies in which we systematically varied key physical and geometric parameters, we demonstrated robustness of model parameters. Specifically, we discovered that the fitting parameters of the vortex sheet model distributed within a small range as we varied the speed of the flow and the width of the computational domain. The length of the vortex sheets spanned approximately 80% of the zebrafish body length and their separation distances covered approximately 50% of their body width.

Despite the consistent values of the model parameters under a wide range of swimming speeds and channel widths, we cannot exclude variations with the characteristics of the fish, such as its locomotory pattern and body shape. Different locomotory patterns of a swimming fish has been associated with distinct flow fields (Lighthill, 1975), thereby requiring a unique set of modeling parameters. Similarly, a variation in the fish body shape might alter the flow field and affect the model parameters. For example, fish with a larger body length-to-width ratio could be modeled more accurately by shorter vortex sheets with a larger separation distance. Dipole- and vortex sheet-based models neglect the wake flow generated by the fish, which was found to have a marginal role on the mean flow field for sufficiently high swimming speeds. We acknowledge, however, that unsteady flow events, such as Karman vortex streets, significantly modulate the locomotory patterns of fish. By maximizing their lateral movements, fish could achieve upstream swimming through reduced muscle activities (Liao, Beal, Lauder and Triantafyllou, 2003; Liao, 2004). A recent study has demonstrated that while swimming in a side-by-side "phalanx" pattern, the interaction between the wake flow generated within a fish school could modify the energy expenditure of the entire school (Ashraf, Bradshaw, Ha, Halloy, Godoy-Diana and Thiria, 2017). Likewise, an improved understanding of the unsteady wake flow could also be critical to elucidating the mechanisms underpinning burst-and-coast swimming patterns (Verhagen, 2004).

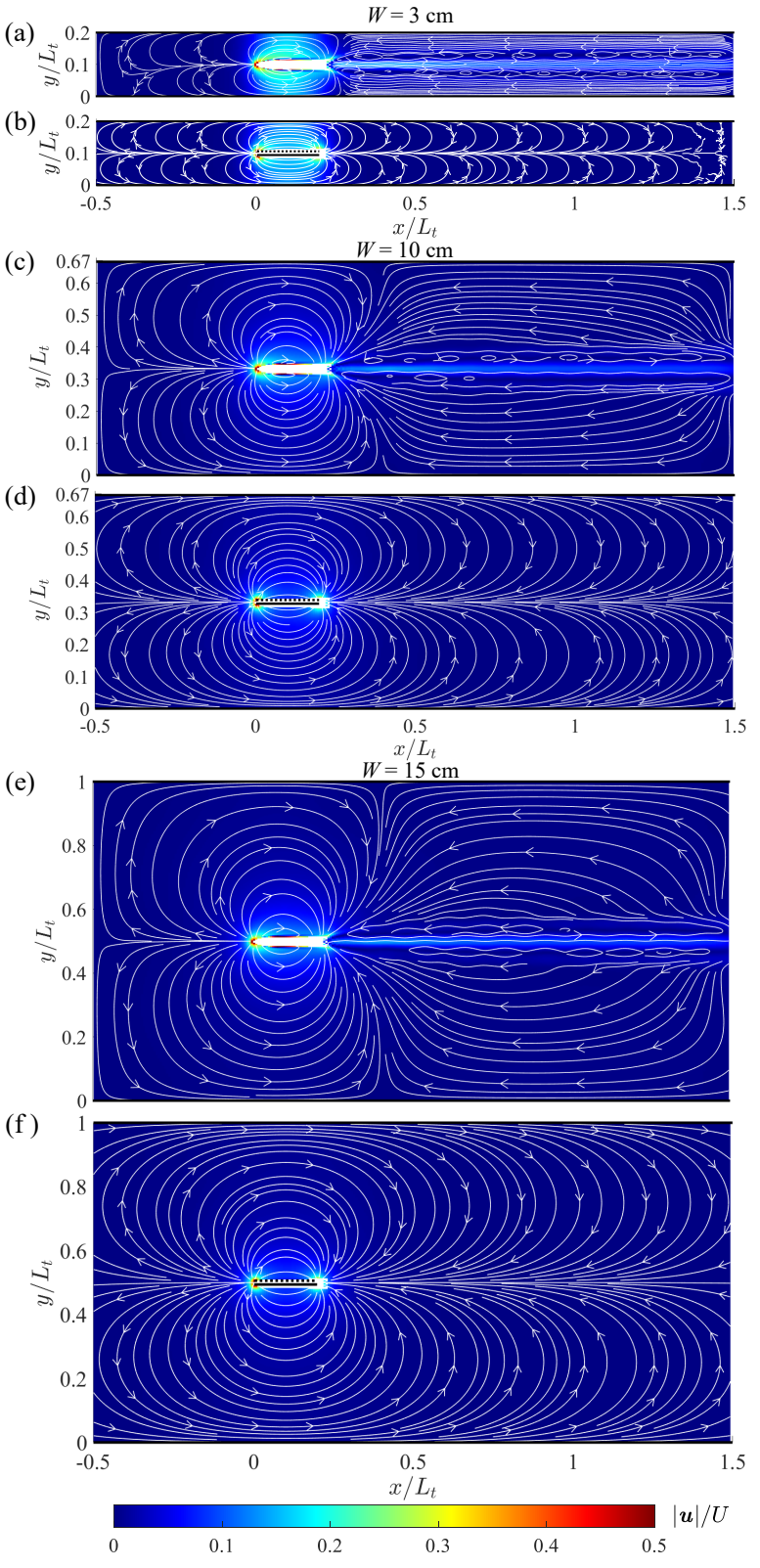

Figure 9: Computational results of the time averaged flow fields around a fish swimming in a channel of width (a) $W = 3\,\mathrm{cm}$, (c) $W = 10\,\mathrm{cm}$, and (e) $W = 15\,\mathrm{cm}$. The corresponding velocity fields fitted by the vortex sheet-based model are displayed in (b), (d), and (f), respectively. Color represents the velocity magnitude scaled by the corresponding swimming speed, $|\boldsymbol{u}|/U$, and white curves and arrows represent velocity streamlines and directions.

The vortex sheet-based model could potentially be amended to mitigate the issue of lack of unsteady phenomena. Free vortex sheets that are allowed to advect in the flow could be superimposed to the flow to capture the wake flow generated by the fish. This configuration of combined bound vortex sheets with free vortex sheets is similar to the one employed in Nitsche and Krasny (1994), where flow generated by a moving object was modeled by "bound" vortex sheets, while vortices shed into the wake were modeled by free vortex sheets. The shedding of the free vortex sheets from the bound vortex sheets could be accomplished according to the Kutta condition (Wu, 2011). Once shed, the free vortex sheet could be advected and interact with another individual positioned in the downstream.

The flexibility of the dipole- and vortex sheet-based models could facilitate the study of fish swimming under more complex flow conditions, such as swimming in the wake of an obstacle or in the vicinity of another fish. As a first approximation, these conditions will require a modification of the background flow only, without affecting the model parameters of the pairs or sheets of vortices. Interestingly, the two-dimensional vortex sheet-based model original to this work could be extended to model swimming in three-dimensions. Two parallel vortex sheets with a finite length and width could be employed to produce the fluid flow around a fish swimming in three-dimensional space. Within this representation, the pair of vortex sheets will be described by their size, orientation, location, separation distance, and circulation density – all parameters to be identified through calibration based on three-dimensional CFD simulations.

Employing the vortex sheet-based model in the study of hydrodynamic interactions will also require extending the concepts of "A-dipole" and "T-dipole" originally proposed by Tchieu et al. (2012) to distributed vorticity. For dipole-based models, these concepts allow for a simple representation of fish response to a background flow. A fish swimming as an A-dipole will respond to a cross flow that contains a gradient along the fish body, similar to the behavior of a slender body. On the contrary, a fish swimming like a T-dipole will rotate according to a gradient in the axial flow across the width of the fish body, like a bluff body. How these concepts extend to distributed vorticity is presently unclear. We believe that CFD of additional flow conditions with targeted flow gradients and estimation of lift and torque on the animal could be of critical guidance to extend A- and T-dipole concepts to a vortex sheet, as function of the specific geometry and swimming patterns of the selected fish species. These simulations could also be integrated with experiments involving robotic fish, where one could control the motion of the robot and measure force resultant acting on it (Chen, Shatara and Tan, 2010).

Funding

This work was supported by the National Science Foundation under Grant No. CMMI-1901697.

Acknowledgements

The authors would like to thank the NYU IT High Performance Computing team for their resources, services, and staff expertise. We specifically thank Shenglong Wang from the NYU HPC team for his help setting up COMSOL Multiphysics simulations on the NYU HPC cluster.

Declaration of interest

The authors declare no competing interests.

CRediT authorship contribution statement

Peng Zhang: Conceptualization, Formal analysis, Investigation, Methodology, Software, Validation, Visualization, Roles/Writing - original draft, Writing - review & editing. **Sean D. Peterson:** Conceptualization, Formal analysis, Funding acquisition, Investigation, Methodology, Project administration, Supervision, Validation, Writing - review & editing. **Maurizio Porfiri:** Conceptualization, Formal analysis, Funding acquisition, Investigation, Methodology, Project administration, Supervision, Validation, Writing - review & editing.

Appendix

A. Vortex sheets with nonuniform circulation density

Here, we investigate the accuracy of vortex sheets with nonuniform circulation density in capturing the flow around a swimming fish. We relaxed the hypothesis of uniform circulation density introduced in Sec. 3.3, and represented it by

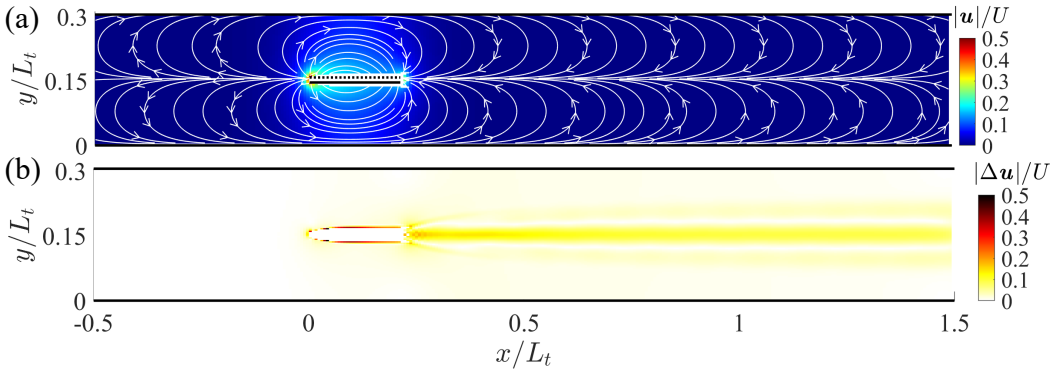

Figure A.1: (a) Velocity field predicted by the vortex sheet-based model with varying circulation density in the absence of a background flow. Color represents the velocity magnitude scaled by the swimming speed, $|\boldsymbol{u}|/U$, and white curves and arrows represent velocity streamlines and directions. (b) Discrepancy between the model predictions and CFD simulations. Color represents magnitude of error scaled by the swimming speed, $|\Delta\boldsymbol{u}|/U$.

a third-order polynomial. Such a representation was chosen to capture tenable velocity variation along the fish body, featuring a high speed region near the head and tail, and a low speed region at the center (see Fig. 6(a)). For a pair of vortex sheets aligned horizontally along the channel, the circulation density of sheet $\mathcal{C}_-$ can be expressed as

$$\gamma(\boldsymbol{x}_-) = \gamma_0 \left(1 + a_1\bar{x} + a_2\bar{x}^2 + a_3\bar{x}^3\right), \tag{A.1}$$

where $\bar{x} = \frac{x-x_0}{L/2}$ was a nondimensional coordinate defined along the sheet with $\bar{x} = -1$ and $\bar{x} = 1$ corresponding to the left and right ends, respectively. Coefficients γ_0, a_1, a_2, and a_3 in Eq. (A.1) were unknown coefficients constants. Along with $\boldsymbol{x}_0$, r_0, and $\mathcal{L}$, these constants were treated as fitting parameters and were determined through calibration against CFD simulations, following a similar procedure detailed in Sec. 3.3. We retained the assumption that $\mathcal{C}_+$ and $\mathcal{C}_-$ have equal and opposite circulation densities, that is, $\gamma(\boldsymbol{x}_+) = -\gamma(\boldsymbol{x}_-)$.

The velocity field predicted by nonuniform vortex sheets is presented in Fig. A.1(a). Similar to uniform vortex sheets, the predicted velocity field captured the elongated streamline patterns from the head to the tail. Discrepancies between model predictions and numerical simulations were noted only within the boundary layer at the body surface and in the wake flow (see Fig. A.1(b)). A relative error of $E/U = 3.07\%$ was registered for the nonuniform vortex sheets, corresponding to a modest 2.6% improvement in accuracy compared with predictions obtained with uniform vortex sheets ($E/U = 3.16\%$).

Compared with uniform vortex sheets, the nonuniform vortex sheets were found to be slightly longer, spanning 89% of the fish body length and covering nearly the entire frontal region. The separation distance between the two vortex sheets was approximately 46% of the body width. The unknown coefficients in Eq. (A.1) were determined as $\gamma_0 = 0.452\,\mathrm{m/s}$, $a_1 = -0.35$, $a_2 = -0.55$, and $a_3 = 0.25$. This corresponded to a variation in the circulation density that peaked near the center of the sheet and reduced near the head and the tail, as shown in Fig. A.2. The total circulation of the nonuniform vortex sheets was approximately $0.0117\,\mathrm{m}^2/\mathrm{s}$, which was close to the total circulation of the uniform vortex sheets of $0.0110\,\mathrm{m}^2/\mathrm{s}$.

References

Adkins, D., Yan, Y., 2006. CFD simulation of fish-like body moving in viscous liquid. Journal of Bionic Engineering 3, 147–153. doi:10.1016/S1672-6529(06)60018-8.

Aref, H., Siggia, E.D., 1981. Evolution and breakdown of a vortex street in two dimensions. Journal of Fluid Mechanics 109, 435–463. doi:10.1017/S0022112081001158.

Ashraf, I., Bradshaw, H., Ha, T.T., Halloy, J., Godoy-Diana, R., Thiria, B., 2017. Simple phalanx pattern leads to energy saving in cohesive fish schooling. Proceedings of the National Academy of Sciences 114, 9599–9604. doi:10.1073/pnas.1706503114.

Ashurst, W.T., Meiburg, E., 1988. Three-dimensional shear layers via vortex dynamics. Journal of Fluid Mechanics 189, 87–116. doi:10.1017/S0022112088000928.

Burbano-L., D.A., Porfiri, M., 2021. Modeling multi-sensory feedback control of zebrafish in a flow. PLoS Computational Biology 17, 1–25. doi:10.1371/journal.pcbi.1008644.

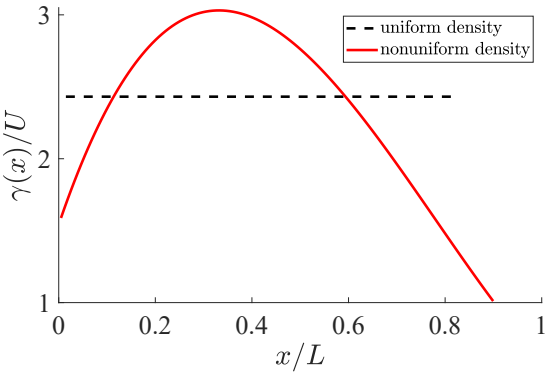

Figure A.2: Optimal distribution of the circulation density for uniform and nonuniform vortex sheets. The uniform vortex sheets corresponded to a total circulation of $0.0110\,\mathrm{m}^2/\mathrm{s}$, while the nonuniform sheets corresponded to a total circulation of $0.0117\,\mathrm{m}^2/\mathrm{s}$.

Chen, Z., Shatara, S., Tan, X., 2010. Modeling of biomimetic robotic fish propelled by an ionic polymer-metal composite caudal fin. IEEE/ASME Transactions on Mechatronics 15, 448–459. doi:10.1109/TMECH.2009.2027812.

Cheng, J.Y., Blickhan, R., 1994. Bending moment distribution along swimming fish. Journal of Theoretical Biology 168, 337–348. doi:10.1006/jtbi.1994.1114.

Coombs, S., Bak-Coleman, J., Montgomery, J., 2020. Rheotaxis revisited: a multi-behavioral and multisensory perspective on how fish orient to flow. Journal of Experimental Biology 223, jeb223008. doi:10.1242/jeb.223008.

Curatolo, M., Teresi, L., 2016. Modeling and simulation of fish swimming with active muscles. Journal of Theoretical Biology 409, 18–26. doi:10.1016/j.jtbi.2016.08.025.

Doi, K., Takagi, T., Mitsunaga, Y., Torisawa, S., 2021. Hydrodynamical effect of parallelly swimming fish using computational fluid dynamics method. PLoS ONE 16, 1–18. doi:10.1371/journal.pone.0250837.

Filella, A., Nadal, F., Sire, C., Kanso, E., Eloy, C., 2018. Model of collective fish behavior with hydrodynamic interactions. Physical Review Letters 120, 198101. doi:10.1103/PhysRevLett.120.198101.

Gazzola, M., Tchieu, A.A., Alexeev, D., de Brauer, A., Koumoutsakos, P., 2016. Learning to school in the presence of hydrodynamic interactions. Journal of Fluid Mechanics 789, 726–749. doi:10.1017/jfm.2015.686.

Hamlet, C., Fauci, L.J., Tytell, E.D., 2015. The effect of intrinsic muscular nonlinearities on the energetics of locomotion in a computational model of an anguilliform swimmer. Journal of Theoretical Biology 385, 119–129. doi:10.1016/j.jtbi.2015.08.023.

Hassan, E.S., 1985. Mathematical analysis of the stimulus for the lateral line organ. Biological Cybernetics 52, 23–36. doi:10.1007/BF00336932.

Hemelrijk, C., Reid, D., Hildenbrandt, H., Padding, J., 2015. The increased efficiency of fish swimming in a school. Fish and Fisheries 16, 511–521. doi:10.1111/faf.12072.

Higdon, J.J.L., Pozrikidis, C., 1985. The self-induced motion of vortex sheets. Journal of Fluid Mechanics 150, 203–231. doi:10.1017/S0022112085000106.

Hunter, J.R., 1969. Communication of velocity changes in jack mackerel (*Trachurus symmetricus*) schools. Animal Behaviour 17, 507–514. doi:10.1016/0003-3472(69)90154-7.

Iosilevskii, G., 2016. Locomotion of neutrally buoyant fish with flexible caudal fin. Journal of Theoretical Biology 399, 159–165. doi:10.1016/j.jtbi.2016.04.001.

Kanso, E., Tsang, A.C.H., 2014. Dipole models of self-propelled bodies. Fluid Dynamics Research 46, 061407. doi:10.1088/0169-5983/46/6/061407.

Katz, J., Weihs, D., 1978. Hydrodynamic propulsion by large amplitude oscillation of an airfoil with chordwise flexibility. Journal of Fluid Mechanics 88, 485–497. doi:10.1017/S0022112078002220.

Kern, S., Koumoutsakos, P., 2006. Simulations of optimized anguilliform swimming. Journal of Experimental Biology 209, 4841–4857. doi:10.1242/jeb.02526.

Khan, A.H., Ruiz Hussmann, K., Powalla, D., Hoerner, S., Kruusmaa, M., Tuhtan, J.A., 2022. An open 3D CFD model for the investigation of flow environments experienced by freshwater fish. Ecological Informatics 69, 101652. doi:10.1016/j.ecoinf.2022.101652.

Liao, J.C., 2004. Neuromuscular control of trout swimming in a vortex street: implications for energy economy during the Kármán gait. Journal of Experimental Biology 207, 3495–3506. doi:10.1242/jeb.01125.

Liao, J.C., 2007. A review of fish swimming mechanics and behaviour in altered flows. Philosophical Transactions of the Royal Society B: Biological Sciences 362, 1973–1993. doi:10.1098/rstb.2007.2082.

Liao, J.C., Beal, D.N., Lauder, G.V., Triantafyllou, M.S., 2003. Fish exploiting vortices decrease muscle activity. Science 302, 1566–1569. doi:10.1126/science.1088295.

Lighthill, M.J., 1970. Aquatic animal propulsion of high hydromechanical efficiency. Journal of Fluid Mechanics 44, 265–301. doi:10.1017/S0022112070001830.

Lighthill, M.J., 1971. Large-amplitude elongated-body theory of fish locomotion. Proceedings of the Royal Society of London. Series B. Biological Sciences 179, 125–138. doi:10.1098/rspb.1971.0085.

Lighthill, S.J., 1975. Mathematical biofluiddynamics. Society for Industrial and Applied Mathematics.

Liu, J., Hu, H., 2010. Biological inspiration: from carangiform fish to multi-joint robotic fish. Journal of Bionic Engineering 7, 35–48. doi:10.1016/S1672-6529(09)60184-0.

Ming, T., Jin, B., Song, J., Luo, H., Du, R., Ding, Y., 2019. 3D computational models explain muscle activation patterns and energetic functions of internal structures in fish swimming. PLoS Computational Biology 15, 1–18. doi:10.1371/journal.pcbi.1006883.

Mwaffo, V., Zhang, P., Cruz, S.R., Porfiri, M., 2017. Zebrafish swimming in the flow: a particle image velocimetry study. PeerJ 5, e4041. doi:10.7717/peerj.4041.

Newton, P.K., 2011. The N-vortex Problem: Analytical Techniques. volume 145. Springer Science & Business Media.

Nitsche, M., Krasny, R., 1994. A numerical study of vortex ring formation at the edge of a circular tube. Journal of Fluid Mechanics 276, 139–161. doi:10.1017/S0022112094002508.

Pavlov, D., Kasumyan, A., 2000. Patterns and mechanisms of schooling behavior in fish: a review. Journal of Ichthyology 40, S163–S231.

Pitcher, T.J., 1998. Shoaling and schooling behavior in fishes. Comparative Psychology: A Handbook. New York, NY: Routledge , 748–60.

Pitcher, T.J., Partridge, B.L., Wardle, C.S., 1976. A blind fish can school. Science 194, 963–965. doi:10.1126/science.982056.

Porfiri, M., Karakaya, M., Sattanapalle, R.R., Peterson, S.D., 2021. Emergence of in-line swimming patterns in zebrafish pairs. Flow 1, E7. doi:10.1017/flo.2021.5.

Porfiri, M., Zhang, P., Peterson, S.D., 2022. Hydrodynamic model of fish orientation in a channel flow. eLife 11, e75225. doi:10.7554/eLife.75225.

Reid, D.A.P., Hildenbrandt, H., Padding, J.T., Hemelrijk, C.K., 2012. Fluid dynamics of moving fish in a two-dimensional multiparticle collision dynamics model. Physical Review E 85, 021901. doi:10.1103/PhysRevE.85.021901.

Saffman, P.G., 1993. Vortex Dynamics. Cambridge Monographs on Mechanics, Cambridge University Press. doi:10.1017/CBO9780511624063.

Sfakiotakis, M., Lane, D., Davies, J., 1999. Review of fish swimming modes for aquatic locomotion. IEEE Journal of Oceanic Engineering 24, 237–252. doi:10.1109/48.757275.

Takagi, T., Tamura, Y., Weihs, D., 2013. Hydrodynamics and energy-saving swimming techniques of pacific bluefin tuna. Journal of Theoretical Biology 336, 158–172. doi:10.1016/j.jtbi.2013.07.018.

Tchieu, A.A., Kanso, E., Newton, P.K., 2012. The finite-dipole dynamical system. Proceedings of the Royal Society A: Mathematical, Physical and Engineering Sciences 468, 3006–3026. doi:10.1098/rspa.2012.0119.

Triantafyllou, M.S., Triantafyllou, G.S., Yue, D.K.P., 2000. Hydrodynamics of fishlike swimming. Annual Review of Fluid Mechanics 32, 33–53. doi:10.1146/annurev.fluid.32.1.33.

Tytell, E.D., Hsu, C.Y., Williams, T.L., Cohen, A.H., Fauci, L.J., 2010. Interactions between internal forces, body stiffness, and fluid environment in a neuromechanical model of lamprey swimming. Proceedings of the National Academy of Sciences 107, 19832–19837. doi:10.1073/pnas.1011564107.

Verhagen, J.H., 2004. Hydrodynamics of burst swimming fish larvae; a conceptual model approach. Journal of Theoretical Biology 229, 235–248. doi:10.1016/j.jtbi.2004.03.022.

Vorus, W.S., Taravella, B.M., 2011. Anguilliform fish propulsion of highest hydrodynamic efficiency. Journal of Marine Science and Application 10, 163–174. doi:10.1007/s11804-011-1056-3.

Windsor, S.P., Norris, S.E., Cameron, S.M., Mallinson, G.D., Montgomery, J.C., 2010a. The flow fields involved in hydrodynamic imaging by blind mexican cave fish (*Astyanax fasciatus*). Part I: open water and heading towards a wall. Journal of Experimental Biology 213, 3819–3831. doi:10.1242/jeb.040741.

Windsor, S.P., Norris, S.E., Cameron, S.M., Mallinson, G.D., Montgomery, J.C., 2010b. The flow fields involved in hydrodynamic imaging by blind mexican cave fish (*Astyanax fasciatus*). Part II: gliding parallel to a wall. Journal of Experimental Biology 213, 3832–3842. doi:10.1242/jeb.040790.

Wolfgang, M., Anderson, J., Grosenbaugh, M., Yue, D., Triantafyllou, M., 1999. Near-body flow dynamics in swimming fish. Journal of Experimental Biology 202, 2303–2327. doi:10.1242/jeb.202.17.2303.

Wu, T.Y., 2011. Fish swimming and bird/insect flight. Annual Review of Fluid Mechanics 43, 25–58. doi:10.1146/annurev-fluid-122109-160648.

Wu, T.Y.T., 1971. Hydromechanics of swimming propulsion. Part 1. swimming of a two-dimensional flexible plate at variable forward speeds in an inviscid fluid. Journal of Fluid Mechanics 46, 337–355. doi:10.1017/S0022112071000570.

Ysasi, A., Kanso, E., Newton, P.K., 2011. Wake structure of a deformable Joukowski airfoil. Physica D: Nonlinear Phenomena 240, 1574–1582. doi:10.1016/j.physd.2011.06.021.